Journal of Materials Chemistry A

PAPER

View Article Online
View Journal | View Issue

Cite this: J. Mater. Chem. A, 2014, 2, 20629

Hierarchically structured TiO_2 for Ba-filled skutterudite with enhanced thermoelectric performance

Xiaoyuan Zhou,*[ac] Guiwen Wang,[ab] Lijie Guo,[a] Hang Chi,[c] Guoyu Wang,*[bc] Qifeng Zhang,[d] Changqiang Chen,[e] Travis Thompson,[f] Jeff Sakamoto,[f] Vinayak P. Dravid,[e] Guozhong Cao[d] and Ctirad Uher*[c]

Received 5th October 2014
Accepted 29th October 2014

DOI: 10.1039/c4ta05285d

www.rsc.org/MaterialsA

The influence of hierarchical TiO_2 inclusions on electrical and thermal transport properties has been investigated in the Ba-filled skutterudite compound $Ba_{0.3}Co_4Sb_{12}$ synthesized by ball milling followed by hot pressing. The hierarchical TiO_2, with the morphology of nanocrystallite aggregates, was prepared using a carbon sphere-templated method. It was found that TiO_2 inclusions strongly enhance the Seebeck coefficient while they weakly degrade the electric conductivity. In addition, TiO_2 inclusions reduce significantly the lattice thermal conductivity through all-scale length phonon scattering due to the hierarchically-structured TiO_2 particles. ZT values up to 1.2 were obtained for $Ba_{0.3}Co_4Sb_{12}$ with an optimal amount and dispersion of TiO_2 inclusions. These observations demonstrate an exciting scientific opportunity to raise the figure-of-merit of filled skutterudites *via* hierarchical dispersion.

Introduction

The world we are living in has been stressed by the rapid growth in energy consumption and its associated environmental problems. To solve these problems, or at least mitigate their influence, the new green energy policies and the more efficient ways we use the energy, should be considered. Thermoelectric (TE) materials are a very good candidate to achieve a more efficient usage of energy, especially in the area of waste industrial heat.[1–7] The figure of merit, ZT, defined as $ZT = S^2\sigma T/\kappa$, where S is the Seebeck coefficient, σ is the electrical conductivity, κ is the thermal conductivity, and T is the absolute temperature, is the parameter which describes the performance of a TE material. The electronic performance of a thermoelectric material is governed by its power factor $P = S^2\sigma$. The challenge to develop efficient TE materials is to achieve a simultaneous enhancement in the power factor while maintaining as low a thermal conductivity as possible.

Among promising thermoelectric materials, filled skutterudites based on $CoSb_3$ have attracted wide attention not only because of their promising dimensionless figure-of-merit, but also because of their very good mechanical properties.[8–18] Current strategies to improve the figure of merit of $CoSb_3$-based filled skutterudites focus on maximizing the power factor through substitutional doping, optimal filling, and reducing the thermal conductivity using mass fluctuation phonon scattering *via* solid-solution alloying. A higher ZT of 1.7 at 850 K, which is the record figure of merit to date for $CoSb_3$-based skutterudites, was realized with multiple co-fillers Ba, La, and Yb.[10]

Another promising approach is to form bulk nanocomposites where various forms of nanoinclusions are dispersed in the $CoSb_3$-based matrix. Provided the phonon mean-free path is reduced by enhanced phonon boundary scattering to a greater degree than any reduction in the mean-free path of charge carriers, the net effect is an improvement in the figure of merit. Moreover, there is also a possibility that the presence of dispersed nanoinclusions will lead to an enhancement in the Seebeck coefficient as a result of energy-dependent scattering of electrons at the interface of nanoinclusions and the matrix.[19–24] Such nanostructured composite materials are fabricated using bulk processing routes rather than nanofabrication means. As such, the synthesis is scalable and compatible with industrial processing.[17] Different kinds of nanoinclusions have been embedded in the skutterudite matrix, among them TiO_2,[20] ZrO_2,[21] NiSb,[22] Yb_2O_3,[23] Ag,[17] C_{60}.[24] They were added to the matrix material *via* mechanical mixing or by *in situ* reaction methods. However, impurities, such as

[a]College of Physics, Chongqing University, Chongqing 401331, People's Republic of China. E-mail: xiaoyuan2013@cqu.edu.cn; guoyuw@cigit.ac.cn; cuher@umich.edu
[b]Chongqing Institute of Green and Intelligent Technology, Chinese Academy of Sciences, Chongqing 400714, People's Republic of China
[c]Department of Physics, University of Michigan, Ann Arbor, MI 48109, USA
[d]Department of Material Science and Engineering, University of Washington, Seattle, WA, 98105, USA
[e]Department of Materials Science and Engineering, Northwestern University, Wilmette, IL, 60091, USA
[f]Department of Chemical Engineering and Materials Science, Michigan State University, East Lansing, MI 48824, USA

oxygen brought by ball milling, exert a negative impact on the electronic transport properties. While the contamination problem can be avoided substantially by using *in situ* reaction methods, the control of composition, grain size and distribution of these *in situ* nanoinclusions is, however, a great challenge. Nevertheless, in view of the fact that the currently achievable thermal conductivity reduction in filled skutterudites is still far from the theoretical limit value of ~0.3 W m^{-1} K^{-1}, further attempts to reduce the thermal conductivity of skutterudites represent worthwhile efforts.

Because the heat in solids is carried by phonons with a rather broad range of wavelengths,[25] it is believed that hierarchically structured thermoelectric materials possessing multi-scale microstructures will have the best chance of greatly reducing the lattice thermal conductivity and thus improving the overall thermoelectric performance. This has been demonstrated with n-type Na-doped PbTe containing MgTe[26] and p-type Na-doped PbSe containing CdS.[27] Here Na doping generates point defects, the second phases form ubiquitous endotaxial nanostructures dispersed in the respective matrices, and the mesoscale microstructure is achieved by spark plasma sintering. Such an all-scale hierarchical structure scatters a broad range of phonons leading to a very low (lattice) thermal conductivity.

In this paper we report on a significantly improved performance of $Ba_{0.3}Co_4Sb_{12}$ achieved by adding hierarchically structured TiO_2 inclusions. This is accomplished because: (a) the Seebeck coefficient is enhanced due to the energy filtering effect whereby the low energy electrons are scattered by the interface of the inclusions and the matrix; (b) the thermal conductivity is greatly reduced by enhanced scattering of a broad range of phonons on hierarchically structured TiO_2 inclusions. These two factors boost the ZT of $Ba_{0.3}Co_4Sb_{12}$ up to 1.2 at 823 K. Our results show clearly that optimal dispersion of the second phase can improve greatly thermoelectric performance.

Experiment

TiO_2 nanocrystallite aggregates were prepared using a carbon sphere-templated method. In a typical fabrication, a precursor sol of TiO_2 was prepared first by dissolving 3.75 mL of titanium isopropoxide in an acidic aqueous solution that contained 2.25 mL of HNO_3 and 7.5 mL of $C_2H_4O_2$ in 15 mL of DI-water. To the as-prepared TiO_2 sol, 5.25 g of sucrose, 1.5 g of cetyltrimethylammonium bromide (CTAB), and 3.75 mL of ethanol were added to obtain a mixture of TiO_2 sol and sucrose plus surfactant. The mixture was then transferred into an autoclave for hydrothermal growth at 225 °C for 10 h. When the temperature of the autoclave cooled down to room temperature naturally, the precipitate was collected and washed several times with water and ethanol through a centrifuge method. The product was dried at 100 °C and the as-received powder was then sintered at 450 °C for 5 h, leading to the formation of TiO_2 nanocrystallite aggregates.

$Ba_{0.3}Co_4Sb_{12}$ was synthesized *via* a solid state reaction followed by ball milling and hot pressing, similar to the process reported in our previous work.[17] Ba (pieces 99.9%), Co (powder 99.5%), and Sb (shot 99.999%) were weighed and placed inside carbon coated quartz ampoules sealed under a vacuum. The sealed ampoules were heated to 1373 K at a rate not exceeding 5 K min^{-1} and kept at that temperature for 5 hours, and then quenched in a supersaturated salt water solution. The resultant samples were further annealed at 1023 K for 7 days. A Retsch P100 ball milling machine was subsequently used to mill the ingots at 300 rpm for 6–8 hours to form the $Ba_{0.3}Co_4Sb_{12}$ powder matrix. Two forms of TiO_2 particles were dispersed into the matrix at 300 rpm for 15 min using a ball milling process. One is TiO_2 nanocrystallite aggregates prepared by a carbon sphere-templated method. The other is commercially available TiO_2 nanoparticles (Degussa Aeroxide P25), which consist of *ca.* 30% rutile and 70% anatase and were used without any purification or treatment. The as-prepared mixture was finally hot pressed at 873 K for 15 minutes. The density of our skutterudite samples is around 7.4 g cm^{-3}, larger than 95% of the theoretical density. It should be noted that: (1) the low temperature and short soaking time of hot pressing are necessary to maintain the TiO_2 nanocrystallite aggregate's structure; (2) ball milling and hot pressing was carried out inside the glove box to prevent oxidation of the prepared powder.

High temperature electrical conductivity (σ) and the Seebeck coefficient (S) were measured on rectangular-shape samples in the interval 300 K to 823 K using a home built apparatus under the protective atmosphere of argon. Thermal diffusivity (λ) was obtained by the laser flash method (Flashline 5000 from Anter), and converted into thermal conductivity (κ) using $\kappa = \lambda C_p d$, where C_p is the specific heat measured using a Netzsch, 404 Pegasus apparatus. Sample density d was calculated from sample dimensions and mass. We use pressure contacts and at all times the sample is under Ar atmosphere to prevent oxidation at elevated temperatures.

X-Ray diffraction patterns for all samples were collected on powders in a Scintag X1 using Cu Kα radiation. Electron-probe microanalysis (EPMA) with a Cameca Camebax EPMA was employed to determine the actual composition of the sintered material. The morphology and microstructure were investigated with field emission scanning electron microscopy (SEM, FEI NOVA) and transmission electron microscopy (JEOL 2100F S/TEM microscope operating at 200 kV accelerating voltage) (Table 1).

Table 1 EPMA data for the sintered skutterudite material containing TiO_2. (The error bar is ~0.02)

Sample	Composition
Matrix	$Ba_{0.22}Co_{3.96}Sb_{12}$
0.5% P25	$Ba_{0.21}Co_{3.95}Sb_{12}Ti_{0.09}O_{0.19}$
0.5% TiO_2 Agg.	$Ba_{0.21}Co_{3.96}Sb_{12}$ $Ti_{0.10}O_{0.19}$
0.5% (TiO_2 Agg. + P25)	$Ba_{0.22}Co_{3.95}Sb_{12}$ $Ti_{0.18}O_{0.37}$
1% TiO_2 Agg.	$Ba_{0.22}Co_{3.96}Sb_{12}$ $Ti_{0.19}O_{0.38}$

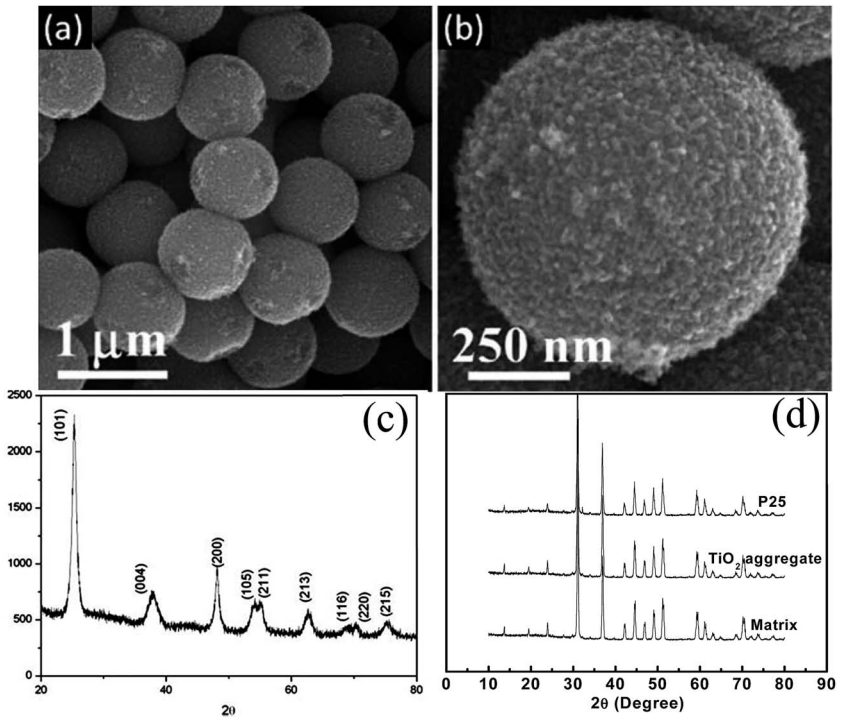

Fig. 1 (a)–(c) SEM images and XRD patterns of TiO_2 nanocrystallite aggregates, (d) XRD patterns of TiO_2-containing Ba-filled skutterudite bulk samples.

Results and discussion

As shown in Fig. 1(a) and (b), the hierarchical structure consists of primary TiO_2 nanocrystallites with a diameter of 12.2 ± 0.3 nm. However, these primary nanostructures form a secondary structure with mesoporous beads typically of 830 ± 40 nm diameter, and a BET surface area of 108.0 $m^2\ g^{-1}$. As shown in Fig. 1(c), TiO_2 nanocrystallite aggregates heat treated at 450 °C for 5 h possess a pure anatase structure, as documented by the peaks indexed to the anatase phase (PDF# 002-0387) without any presence of the rutile and brookite phases. As to the formation mechanism of this hierarchical TiO_2 nanocrystallite aggregates, sucrose is used in this method as a carbon source to generate spherical carbon through a hydrolysis process which occurs at ~180 °C; the spherical carbon works as a template during the growth of TiO_2 nanoparticles, resulting in the formation of spherical aggregates of TiO_2 nanocrystallites. It has been found that the size of the nanocrystallite aggregates is a function of the pH value of the precursor solution, while the size of TiO_2 nanocrystallites is dependent on both the concentration of TiO_2 sol and the temperature adopted for the hydrothermal growth. Sintering at 450 °C was purposely designed and carried out to remove carbon from the product and, meanwhile, improve the crystallinity of the anatase TiO_2.

Powder XRD patterns for these TiO_2-containing Ba-filled skutterudite bulk samples are shown in Fig. 1(d). All major reflections are indexed to the skutterudite phase. No trace of TiO_2 is detected in any sample due to the small volume fraction of TiO_2 inclusions. However, our EPMA data (error bar is around 0.02) clearly reveal the presence of close to the nominal amount of TiO_2. Regarding the Ba content, the actual amounts of Ba in each TiO_2-containing sample are very similar but a bit smaller than the nominal composition. We observe no shift of peaks to higher angles, which we attribute to the relatively short ball milling time and rate that is chosen to minimize the contamination from milling media and prevent the lattice strain build-up during ball milling which might otherwise have a detrimental effect on the electronic mobility.[28–31]

SEM images of the fractured sintered bulk sample containing two different kinds of TiO_2 particles, namely 0.5 wt% P25 plus 0.5 wt% TiO_2 nanocrystallite aggregates are shown in Fig. 2(a) and (b). The bottom left inset of Fig. 2(b) displays the SEM image for Ba-filled skutterudite with 1 wt% TiO_2 nanocrystallite aggregates. These samples possess sharp and clean grain boundaries, which are beneficial for charge transport. In addition, some TiO_2 nanocrystallite aggregates and nanoparticles are observed at the grain boundaries and the surface of the skutterudite sample. Such inclusions are reported to enhance scattering of phonons with mid- to long-wavelengths, as shown schematically in Fig. 2(f), thereby providing a mechanism to reduce significantly the lattice thermal conductivity.[32–38] It is straightforward to identify the inclusions as dispersed TiO_2 aggregates since their size and morphology are very similar to the as-prepared TiO_2 nanocrystallite aggregates. The preservation of the continuous hierarchical structure is clearly evident in a close-up TEM image of TiO_2 aggregates in Fig. 2(c), which shows a single aggregate in the sintered bulk sample. SAED (Selected Area Electron Diffraction) patterns of

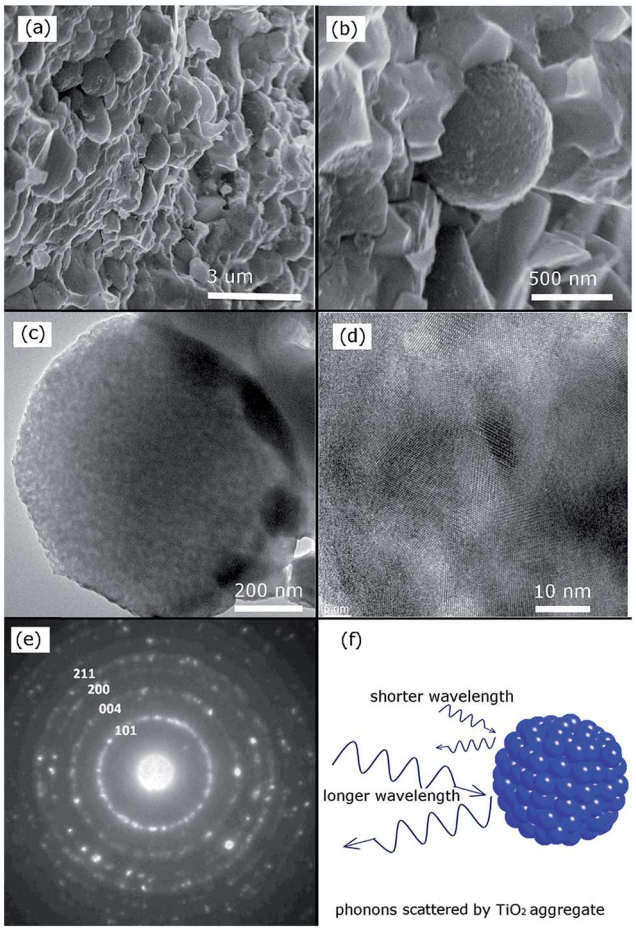

Fig. 2 SEM and TEM micrographs showing TiO_2 aggregates dispersed in the matrix: (a and b) SEM images of Ba-filled skutterudite with aggregates of 0.5% P25 + 0.5% TiO_2. The bottom left inset of (b) is an SEM image of Ba-filled skutterudite with 1% TiO_2 aggregates; (c) a close-up image of TiO_2 sphere; (d and e) SAED (Selected Area Electron Diffraction) patterns and HRTEM imaging of the TiO_2 aggregates; (f) a schematic diagram illustrating various phonon scattering mechanisms taking place on embedded TiO_2 inclusions.

the TiO_2 aggregates, Fig. 2(d), demonstrate that they are composed of TiO_2 nanocrystallites with the anatase structure. HRTEM images show individual nanocrystallites on the scale of 10–20 nm. Unfortunately, until now, we have not been able to provide a single TEM image depicting the presence of commercially-obtained P25 together with TiO_2 nanocrystallite aggregates, likely due to the very small amount of TiO_2 inclusions we employ in our study. Judging from the SEM and TEM images, the size and shape of these TiO_2 nanocrystallite aggregates is unchanged, instead of being enlarged after hot pressing. It should be mentioned that the preservation of the nanocrystallite aggregate structure is critical to ensure the enhanced phonon scattering even after long-term exposure to temperatures where the material will be expected to operate in thermoelectric modules. As such, the hot pressing parameters are not a trivial matter. The processing conditions with respect to the temperature and the soaking time are of prime concern and determine the quality of the final product.

Temperature dependence of the electrical conductivity (σ), the Seebeck coefficient (S), and the power factor ($PF = S^2\sigma$) for Ba-filled skutterudites containing different dispersed forms of TiO_2 inclusions are plotted in Fig. 3. The sample designated as Matrix is a hot-pressed ball-milled powder of $Ba_{0.3}Co_4Sb_{12}$ without TiO_2 inclusions. As shown in Fig. 3(a), all samples display metallic conduction behavior. The electrical conductivity decreases with increasing temperature over the entire temperature range. In addition, TiO_2-containing samples exhibit a lower electrical conductivity than matrix. Specifically, the electrical conductivity decreases from ~3533 S cm^{-1} to ~3199 S cm^{-1} and from 2000 S cm^{-1} to 1600 S cm^{-1} for matrix, respectively, compared to the sample containing 1 wt% TiO_2 nanocrystallite aggregates at room temperature and 823 K. This trend is completely opposite to the case of Ag-containing $Ba_{0.3}Co_4Sb_{12}$,[17] where the electrical conductivity was significantly enhanced by the presence of Ag nanoinclusions. Such a different behavior is due to Ag and TiO_2 being two entirely different kinds of inclusions; that is, Ag is a metal with the highest electrical conductivity while TiO_2 is a wide band gap semiconductor. Ag nanoparticles, dispersed on the surfaces of the grains and at grain boundaries, promote electrical connectivity at the grain boundaries and thus improve electronic transport. In contrast, TiO_2 is electrically inert at experimental temperatures and merely scatter charge carriers, leading to a slight degradation of the electrical conductivity. It is interesting to note that the skutterudite sample containing the commercial form of TiO_2 (P25) has a lower electrical conductivity than the sample containing an equal amount of prepared TiO_2 aggregates. A possible reason for this difference could be the fact that TiO_2 aggregates represent the pure anatase phase while the commercially obtained TiO_2 contains 30% of the rutile phase. It is considered that anatase phase is more desirable for charge transport, allowing for the improvement of electrical conductivity in the TiO_2-aggregate-containing skutterudites.[39]

As shown in Fig. 3(b), all samples have a negative Seebeck coefficient and show an increasing trend with increasing temperature, indicating that the majority carriers are electrons. In contrast to the Seebeck coefficient of −167 μV K^{-1} for the matrix sample, the Seebeck coefficients of −179 and −176 μV K^{-1} were obtained for samples containing 0.5% P25 plus 0.5% TiO_2 aggregates and 0.5% commercial available P25, respectively. The Seebeck coefficient, according to Mott, can be expressed as[38]

$$S = \frac{\pi^2 \kappa_b{}^2 T}{3q}\left(\frac{\mathrm{d}\ln N(E)}{\mathrm{d}E} + \frac{\mathrm{d}\ln \tau(E)\nu(E)^2}{\mathrm{d}E}\right)_{E=E_F}$$

here $N(E)$ and τ are the electronic density of state and the relaxation time, respectively. It is difficult to conclude, based on the electronic transport properties of TiO_2-containing $Ba_{0.3}Co_4Sb_{12}$ whether one also benefits from the first term in the above equation (any sharpening of the density of states at the Fermi level). However, band bending at the interface between embedded nanoinclusions and the semiconducting matrix might produce a scattering potential that could preferentially scatter low energy charge carriers, leading to an enhancement

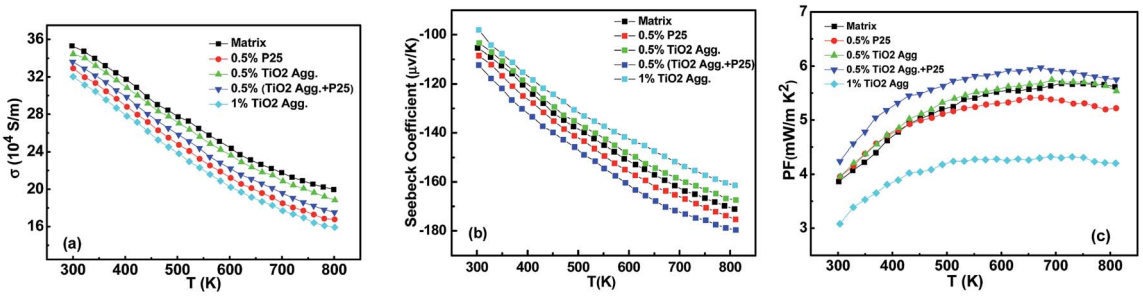

Fig. 3 (a) Electrical conductivity, (b) Seebeck coefficient, and (c) power factor for $Ba_{0.3}Co_4Sb_{12}$ (Matrix) and $Ba_{0.3}Co_4Sb_{12}$ with 0.5% P25, 0.5% TiO_2 aggregates, 0.5% P25 + 0.5% TiO_2 aggregates, and 1% TiO_2 aggregates, respectively.

of the Seebeck coefficient, just as was the case with Pb nanoparticles in PbTe.[40]

The power factor of these samples is plotted in Fig. 3(c). The power factor of the Matrix sample is very close to that of the sample containing 0.5 wt% TiO_2 aggregates over the entire temperature range. The Matrix sample possesses the largest electrical conductivity of all samples, as shown in Fig. 3(a). However, its Seebeck coefficient is inferior to TiO_2-containing samples, and thus the highest power factor is obtained for samples with 0.5% P25 plus 0.5% TiO_2 aggregates, reaching its maximum of 6 mW K^{-2} m^{-1} at around 675 K.

Fig. 4(a) displays the temperature dependence of the thermal conductivity (κ) for samples containing different amounts of TiO_2 inclusions calculated from equation $\kappa = \lambda C_p d$. The matrix sample has the largest thermal conductivity, reaching 4.52 W m^{-1} K^{-1} at 813 K, which is 16%, 5%, 14%, and 14% higher than the samples of $Ba_{0.3}Co_4Sb_{12}$ with additions of 0.5% P25, 0.5% TiO_2 aggregates, 0.5% P25 plus 0.5% TiO_2 aggregates, and 1% TiO_2 aggregates, respectively. As such, embedding TiO_2 inclusions is, indeed, effective in reducing the thermal conductivity of $Ba_{0.3}Co_4Sb_{12}$. Thermal conductivity can be divided into two major components, $\kappa = \kappa_e + \kappa_l$. The electronic component of the thermal conductivity (κ_e) is due to the heat transported by electrons. The lattice component of the thermal conductivity (κ_l) is due to the heat transported by phonons and is low for amorphous or disordered materials. The electronic thermal conductivity was estimated using the Wiedemann–Franz law $\kappa_e = L\sigma T$, where the constant, L, known as the Lorenz number, depends on the degree of elasticity in carrier scattering. We take L at its fully degenerate value of $L = 2.44 \times 10^{-8}$ V^2 K^{-2}, which is believed to be reasonable for our degenerate semiconductors.[17]

The lattice thermal conductivity is calculated by subtracting the electronic part from the total thermal conductivity as shown in Fig. 4(b). Lattice thermal conductivities follow approximately the $1/T$ relation and samples containing TiO_2 inclusions display much reduced values, except for $Ba_{0.3}Co_4Sb_{12}$ with 1% aggregates. A contributing factor in this reduction is the enhanced phonon scattering associated with the presence of TiO_2 inclusions. The heat flow is carried by a spectrum of phonons with a rather broad range of wavelengths. Commercial P25 with a size ranging from ~20–40 nm is an efficient scatterer of shorter wavelength phonons, leading to a much lower lattice thermal conductivity of $Ba_{0.3}Co_4Sb_{12}$-containing 0.5% P25. However, in the case of samples with 0.5% hierarchically structured TiO_2, due to the inclusions being spheres with a diameter of ~600–800 nm, they scatter phonons with longer wavelength preferentially. While the thermal conductivity is reduced, it is decreased to a lesser degree because such phonons carry a smaller fraction of the overall heat. Noticeably, the lowest lattice thermal conductivity is obtained in samples with 0.5% P25 plus 0.5% hierarchically structured TiO_2, reaching 0.50 W m^{-1} K^{-1} at 813 K and reflecting a wider frequency range of phonons that is affected by scattering on inclusions in $Ba_{0.3}Co_4Sb_{12}$. However, when an excessive amount of TiO_2 aggregates, up to 1%, is

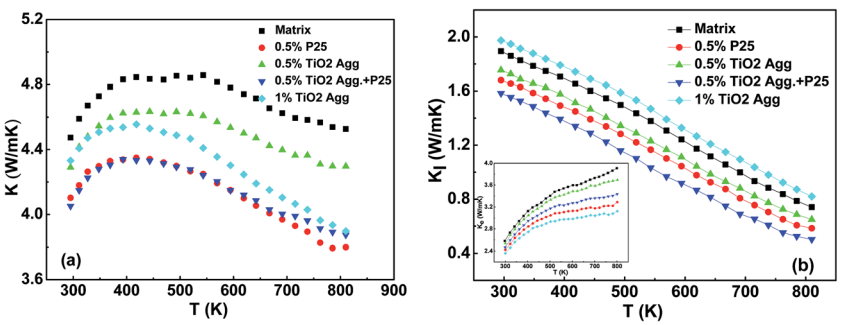

Fig. 4 (a) Thermal conductivity and (b) lattice thermal conductivity for the $Ba_{0.3}Co_4Sb_{12}$ Matrix, and skutterudite samples containing 0.5% P25, 0.5% TiO_2 aggregates, 0.5% P25 + 0.5% TiO_2 aggregates, and 1% TiO_2 aggregates. The inset of (b) shows the corresponding electronic thermal conductivity.

added to $Ba_{0.3}Co_4Sb_{12}$, the lattice thermal conductivity becomes larger than that of the Matrix sample. Therefore, only optimized combinations of inclusions in $Ba_{0.3}Co_4Sb_{12}$, representing equal amounts of P25 and hierarchically structured TiO_2, can reduce the lattice thermal conductivity to the greatest extent. This observation is in a good agreement with our previous study.[17]

The dimensionless thermoelectric figure of merit ZT of our samples is calculated based on the above transport data and is plotted in Fig. 5. It is found that the ZT values increase with the increasing temperature in the measured temperature range. Among samples with different kinds of TiO_2 inclusions, the sample with 0.5% P25 plus 0.5% hierarchically structured TiO_2 aggregates reaches the highest ZT, around 1.20 at ~813 K. This is approximately 12%, 9%, 20% and 40% higher than the ZT value of the Matrix, and $Ba_{0.3}Co_4Sb_{12}$ containing 0.5% P25, 0.5% and 1% TiO_2 aggregates, respectively. The improvement in the figure of merit is attributed to: (a) embedded TiO_2 inclusions which provide extra phonon scattering centers and lower the lattice thermal conductivity; (b) the energy filtering effect caused by the interface between nanoinclusions and the matrix which enhances the Seebeck coefficient. This simultaneous enhancement in the Seebeck coefficient and the diminished heat conduction ability of phonons results in an improved thermoelectric figure of merit of $Ba_{0.3}Co_4Sb_{12}$ containing TiO_2 inclusions, in spite of the reduced electrical conductivity in these samples.

Conclusion

$Ba_{0.3}Co_4Sb_{12}$ samples containing hierarchically structured TiO_2 were synthesized by ball milling and subsequent hot press sintering. They show a very good thermoelectric performance with the highest ZT value reaching 1.2 at 813 K when 0.5% P25 plus 0.5% TiO_2 aggregates are added to the $Ba_{0.3}Co_4Sb_{12}$ matrix. The TiO_2 nanocrystallite aggregates were prepared using a carbon sphere-templated method. It is found that TiO_2 inclusions are dispersed between the grain boundaries and on the surfaces of grains. The observed enhancement in the Seebeck coefficient together with a significant reduction in the thermal conductivity leads to an improved ZT in these $TiO_2/Ba_{0.3}Co_4Sb_{12}$ bulk composite structures. This method is a good example of optimizing inclusions to achieve desirable thermoelectric properties in n-type Ba-filled skutterudites.

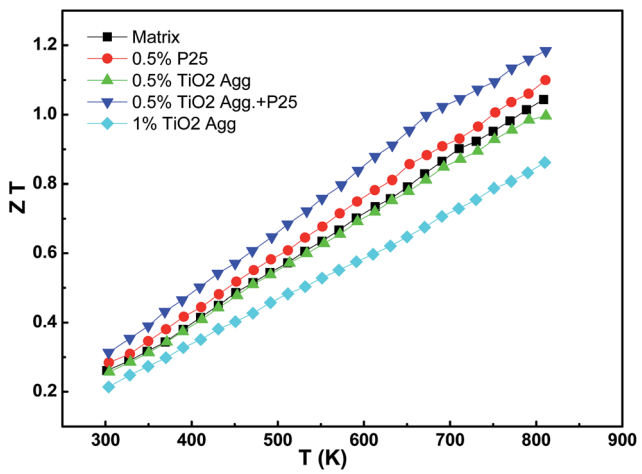

Fig. 5 ZT for the $Ba_{0.3}Co_4Sb_{12}$ Matrix and skutterudite samples containing 0.5% P25, 0.5% TiO_2 aggregates, 0.5% P25 + 0.5% TiO_2 aggregates, and 1% TiO_2 aggregates, respectively.

Acknowledgements

The work was financially supported in part by the National Natural Science Foundation of China (Grant no. 11344010), the Fundamental Research Funds for the Central Universities (CQDXWL-2013-Z010). Experimental studies at the University of Michigan were supported by the Revolutionary Materials for Solid State Energy Conversion, an Energy Frontier Research Center funded by the US Department of Energy, Office of Science, Office of Basic Energy Science under Award Number DE-SC001054. The work at the Chongqing Institute of Green and Intelligent Technology, Chinese Academy of Sciences is supported by the One Hundred Person Project of the Chinese Academy of Science, Grant no. 2013-46.

References

1 C. Uher, in *Semiconductors and Semimetals*, ed. T. M. Tritt, Academic Press, San Diego, 2001, vol. 69, pp. 139–253.
2 T. Caillat, A. Borshchevsky and J. P. Fleurial, *J. Appl. Phys.*, 1996, **80**, 4442.
3 B. X. Chen, J. H. Xu, C. Uher, D. T. Morelli, G. P. Meisner, J. P. Fleurial, T. Caillat and A. Borshchevsky, *Phys. Rev. B: Condens. Matter*, 1997, **55**, 1476.
4 L. D. Chen, T. Kawahara, X. F. Tang, T. Goto, T. Hirai, J. S. Dyck, W. Chen and C. Uher, *J. Appl. Phys.*, 2001, **90**, 1864.
5 H. Li, X. Tang, Q. Zhang and C. Uher, *Appl. Phys. Lett.*, 2009, **94**, 102114.
6 H. Li, X. F. Tang, Q. J. Zhang and C. Uher, *Appl. Phys. Lett.*, 2008, **93**, 252109.
7 D. T. Morelli and G. P. Meisner, *J. Appl. Phys.*, 1995, **77**, 3777.
8 X. L. Su, H. Li, Y. G. Yan, H. Chi, X. F. Tang, Q. J. Zhang and C. Uher, *J. Mater. Chem.*, 2012, **22**, 15628.
9 Y. T. Qiu, L. L. Xi, X. Shi, P. F. Qiu, W. Q. Zhang, L. D. Chen, J. R. Salvador, J. Y. Cho, J. H. Yang, Y. C. Chien, S. W Chen, Y. L. Tang and G. J. Snyder, *Adv. Funct. Mater.*, 2013, **23**, 3194.
10 X. Shi, J. Yang, J. R. Salvador, M. F. Chi, J. Y. Cho, H. Wang, S. Q. Bai, J. H. Yang, W. Q. Zhang and L. D. Chen, *J. Am. Chem. Soc.*, 2011, **133**, 7837–7846.
11 G. S. Nolas, D. T. Morelli and T. M. Tritt, *Annu. Rev. Mater. Sci.*, 1999, **29**, 89.
12 G. S. Nolas, M. Kaeser, R. T. Littleton and T. M. Tritt, *Appl. Phys. Lett.*, 2000, **77**, 1855.
13 B. C. Sales, D. Mandrus and R. K. Williams, *Science*, 1996, **272**, 1325.
14 J. R. Salvador, J. Yang, X. Shi, H. Wang, A. A. Wereszczak, H. Kong and C. Uher, *Philos. Mag.*, 2009, **89**, 1517.
15 X. Shi, H. Kong, C. P. Li, C. Uher, J. Yang, J. R. Salvador, H. Wang, L. Chen and W. Zhang, *Appl. Phys. Lett.*, 2008, **92**, 182101.

16 G. Rogl and P. Rogl, *Sci. Adv. Mater.*, 2011, **3**, 517.
17 X. Y. Zhou, G. Y. Wang, L. Zhang, H. Chi, X. L. Su, J. Sakamoto and C. Uher, *J. Mater. Chem.*, 2012, **22**, 2958.
18 J. Zhou, X. B. Li, G. Chen and R. G. Yang, *Phys. Rev. B: Condens. Matter Mater. Phys.*, 2010, **82**, 115308.
19 Z. M. He, C. Stiewe, D. Platzek, G. Karpinski and E. Müller, *J. Appl. Phys.*, 2007, **101**, 043707.
20 D. Cederkrantz, N. Farahi, K. A. Borup, B. B. Iversen, M. Nygren and A. E. C. Palmqvist, *J. Appl. Phys.*, 2012, **111**, 023701.
21 X. Y. Huang, Z. Xu and L. D. Chen, *Solid State Commun.*, 2004, **130**, 181.
22 S. Katsuyama, M. Watanabe, M. Kuroki, T. Maehata and M. Ito, *J. Appl. Phys.*, 2003, **93**, 2758.
23 L. D. Chen, X. Y. Huang, M. Zhou, X. Shi and W. B. Zhang, *J. Appl. Phys.*, 2006, **99**, 064305.
24 F. Brochin, B. Lenoir, X. Devaux, R. Martin-Lopez and H. Scherrer, *J. Appl. Phys.*, 2000, **88**, 3269.
25 G. J. Snyder and E. S. Toberer, *Nat. Mater.*, 2008, **7**, 105.
26 K. Biswas, J. He, I. D. Blum, C. Wu, T. Hogan, D. N. Seidman, V. P. Dravid and M. G. Kanatzidis, *Nature*, 2012, **489**, 414.
27 L. D. Zhao, S. Hao, S. H. Lo, C. I. Wu, X. Y. Zhou, Y. Lee, H. Li, K. Biswas, T. P. Hogan, C. Uher, C. Wolverton, V. P. Dravid and M. G. Kanatzidis, *J. Am. Chem. Soc.*, 2013, **135**, 7364.
28 M. S. Dresselhaus, G. Chen, M. Y. Tang, R. G. Yang, H. Lee, D. Z. Wang, Z. F. Ren, J. P. Fleurial and P. Gogna, *Adv. Mater.*, 2007, **19**, 1043.
29 S. K. Bux, J. P. Fleurial and R. B. Kaner, *Chem. Commun.*, 2010, **46**, 8311.
30 C. J. Vineis, A. Shakouri, A. Majumdar and M. G. Kanatzidis, *Adv. Mater.*, 2010, **22**, 3970.
31 B. Yu, Q. Y. Zhang, H. Wang, X. W. Wang, H. Z. Wang, D. Z. Wang, H. Wang, G. J. Snyder, G. Chen and Z. F. Ren, *J. Appl. Phys.*, 2010, **108**, 016104.
32 M. G. Kanatzidis, *Chem. Mater.*, 2010, **22**, 648.
33 Y. C. Lan, A. J. Minnich, G. Chen and Z. F. Ren, *Adv. Funct. Mater.*, 2010, **20**, 357.
34 W. J. Xie, J. A. He, H. J. Kang, X. F. Tang, S. Zhu, M. Laver, S. Y. Wang, J. R. D. Copley, C. M. Brown, Q. J. Zhang and T. M. Tritt, *Nano Lett.*, 2010, **10**, 3283.
35 P. Vaqueiro and A. V. Powell, *J. Mater. Chem.*, 2010, **20**, 9577.
36 A. J. Minnich, M. S. Dresselhaus, Z. F. Ren and G. Chen, *Energy Environ. Sci.*, 2009, **2**, 466.
37 L. D. Zhao, V. P. Dravid and M. G. Kanatzidis, *Energy Environ. Sci.*, 2014, **7**, 251.
38 D. L. Medlin and G. J. Snyder, *Curr. Opin. Colloid Interface Sci.*, 2009, **14**, 226.
39 Q. F. Zhang, K. Park, J. T. Xi, D. Myers and G. Z. Cao, *Adv. Energy Mater.*, 2011, **1**, 988.
40 J. P. Heremans, C. M. Thrush and D. T. Morelli, *Phys. Rev. B: Condens. Matter Mater. Phys.*, 2004, **70**, 115334.